Storing quantum information for 30 seconds in a nanoelectronic device

Juha T. Muhonen,[1] Juan P. Dehollain,[1] Arne Laucht,[1] Fay E. Hudson,[1] Rachpon Kalra,[1] Takeharu Sekiguchi,[2] Kohei M. Itoh,[2] David N. Jamieson,[3] Jeffrey C. McCallum,[3] Andrew S. Dzurak,[1] and Andrea Morello[1]

[1] *Centre for Quantum Computation and Communication Technology,*
School of Electrical Engineering and Telecommunications,
UNSW Australia, Sydney, New South Wales 2052, Australia
[2] *School of Fundamental Science and Technology,*
Keio University, 3-14-1 Hiyoshi, 223-8522, Japan
[3] *Centre for Quantum Computation and Communication Technology,*
School of Physics, University of Melbourne, Melbourne, Victoria 3010, Australia

A. Summary of the measured coherence times

	Device A			Device B		
	e^-	$^{31}P^0$	^{31}P	e^-	$^{31}P^0$	^{31}P
Ramsey (T_2^*)	270 μs	570 μs	250 ms	160 μs	430 μs	600 ms
Hahn-Echo (T_2^H)	0.95 ms	1.5 ms	580 ms	1.1 ms	20 ms	1.8 s
CPMG (T_2^{CPMG})	220 ms	2.7 ms	1.1 s	550 ms	20 ms	35.6 s

TABLE S1. **Qubit coherence times.** Summary table of the coherence benchmarks for the electron (e^-), the neutral nucleus ($^{31}P^0$) and ionized nucleus () qubits. Note: the value of T_{2n+}^{CPMG} quoted for Device A should not be taken as the limit $^{31}P^+$ coherence time, because only 16 CPMG pulses were applied in that measurement. Device B also had an additional 7 dB attenuation at the 1.5 K stage of the cable connecting to the microwave line.

B. Pulse sequences for qubit operation

The performance of the qubits was measured using the standard magnetic resonance pulse protocols. We define a rotating reference frame where Z is the direction of the static B_0 field, while X and Y rotate around Z at the qubit precession frequency, so they appear static in the reference frame of the qubit. A rotation of the spin by an angle θ around the Φ axis in the rotating reference frame is indicated as Φ_θ. By convention, X is defined by the phase of the first resonant pulse applied to the qubit, whereas a pulse around Y is obtained through a 90° phase shift of the microwave source. Arbitrary quantum states are encoded on the qubits by applying pulses of oscillating magnetic field B_1 at the frequencies corresponding to the electron spin resonance (ESR), $\nu_{e1,2} \approx \gamma_e B_0 \pm A/2$, and nuclear magnetic resonance (NMR), $\nu_{n1,2} \approx A/2 \pm \gamma_n B_0$, where $\gamma_e = 27.97$ GHz/T and $\gamma_n = 17.23$ MHz/T are the electron and nuclear gyromagnetic ratios, respectively, and A is the hyperfine

coupling. The ESR spectra yielded $A/h = 116.6$ MHz for Device A and $A/h = 96.9$ MHz for Device B. The ^{31}P qubit can also be operated at the frequency $\nu_0 = \gamma_n B_0$ while the electron is absent, i.e. the P atom is ionized [1, 2].

All of the measurements described in the main text consist of two phases: a control phase and a readout phase. During the control phase, the donor potential is tuned below (for e^- and $^{31}P^0$) or above (for $^{31}P^+$) the Fermi level of the SET island, to maintain the donor in the neutral or ionized state, respectively, during the application of control pulses. The readout phase follows directly after the control phase and consists of a single-shot electron readout [3] (for e^-), or a single-shot nuclear readout [4] (for ^{31}P). Each measurement is repeated several times to compute the spin-up proportion $P_\uparrow$ (for the electron) or the spin flip probability P_f (for the nucleus).

We applied the following pulse sequences:

(i) Rabi oscillations, obtained by monitoring $P_\uparrow$ (for e^-) or P_f (for ^{31}P) as a function of the duration τ_R of a pulse X_θ, with $\theta = 2\pi\tau_R/\gamma B_1$;

(ii) Ramsey fringes, obtained by applying a $X_{\pi/2}$ pulse, followed by a free precession time τ, then another $X_{\pi/2}$ pulse-pulse that brings the spin back along the Z-axis for measurement ($X_{\pi/2}-\tau-X_{\pi/2}$). $P_\uparrow$ or P_f oscillate if the frequency of the microwave source is detuned from the qubit frequency, and the decay of the oscillations' envelope yields the pure dephasing time T_2^*;

(iii) Hahn echo, obtained by introducing a X_π pulse between the $X_{\pi/2}$ pulses in a Ramsey sequence ($X_{\pi/2} - \tau/2-X_\pi-\tau/2-X_{\pi/2}$). The X_π pulse cancels the effect of random variations of the instantaneous qubit frequency that are static over the timescale of a single experimental run, and yields the qubit coherence time T_2^H;

(iv) Carr-Purcell-Meiboom-Gill (CPMG), where the X_π pulse in the Hahn echo sequence is replaced by N Y_π pulses separated by τ ($X_{\pi/2} - (\tau/2 - Y_\pi - \tau/2)^N - X_{\pi/2}$). This sequence is often used to extend the timescale over which a quantum coherent state can be preserved. The CMPG sequence is immune to imperfections in the Y_π pulses up to fourth order. The decay measurement can be performed in two ways: by fixing N and varying τ, or by fixing τ and varying N. The mea-

surements differ in how the effective noise filter changes after each sequence increment. Here we use the fixed-τ/variable-N sequence to extract the spectrum of the noise that couples to the qubit, and the fixed-N/variable-τ sequence to measure the ultimate limit of T_2. A variant of CPMG is the Carr-Purcell (CP) sequence, where the Y_π pulses are replaced with X_π. This sequence has the same filter function as CPMG, but loses the immunity to pulse errors. Here we use this sequence to extract the control fidelity of the qubits.

In each case, the qubit coherence decays as a function of the total wait time t with a law of the form $P(t) = P_0 \exp\left[-\left(t/T_2\right)^n\right] + P_\infty$. The decay exponent n is related to the frequency dependence of the power spectral density $S(\omega)$ of the noise that couples to the qubit (see noise spectroscopy, section E).

C. Electron spin resonance linewidths

The free induction decay (T_2^*) envelope is intrinsically related to the electron spin resonance lineshape through a Fourier transform. However, to measure the linewidth directly in an ESR spectrum experiment, the excitation profile of the applied microwave must be narrower than the intrinsic linewidth in order to avoid power-broadening.

One method commonly used to narrow the excitation profile in pulsed experiments is to apply pulse shaping. The ESR spectrum of device A was measured using square pulses at -50 dBm of source power. We obtained a linewidth of 3.8 kHz with a Lorentzian shape, indicating the presence of power broadening. The spectral width of the excitation in a pulsed spin resonance experiment can be narrowed using pulse shaping. On device B we measured the ESR linewidth using Gaussian-shaped pulses, which allowed us measure a $\Delta\nu_{\mathrm{FWHM}} = 1.8$ kHz, much closer to the intrinsic linewidth. The lineshape here was Gaussian, consistent with the $n = 2$ exponent of the Ramsey decay. The measured ESR lines are shown in Fig. S1. Note that for Gaussian decay the $\Delta\nu_{\mathrm{FWHM}}$ and T_2^* are related through $\Delta\nu_{\mathrm{FWHM}} = \ln(2)/(\pi T_2^*)$.

The values of $\Delta\nu_{\mathrm{FWHM}}$ we observed are substantially smaller than those measured in bulk ensembles, even in ultra-pure ^{28}Si sourced from the Avogadro Project [5] which contain < 50 ppm residual ^{29}Si. With 800 ppm residual ^{29}Si in our epilayer, the expected number of ^{29}Si nuclei in the 1.1 nm Bohr radius of the electron wave function [6] is less than 1. This brings us in a very peculiar regime where the 'spin bath' is a small and discrete system, mostly made up of distant dipolar-coupled spins, and comparisons with ensemble-averaged experiments are not meaningful. In addition, a single-atom experiment is intrinsically immune from inhomogeneities in the g-factor and the hyperfine coupling. The $n = 2$ decay exponent of the Ramsey oscillations corresponds to a Gaussian lineshape in the frequency domain, as expected for a single spin in a dilute spin bath [7].

D. Measurement and control fidelities

The e$^-$ measurement fidelity is defined as in Ref. [1]. It is extracted from the Rabi oscillation data shown in Fig. S2, and from histograms of the maximum current during readout. From the latter we extract an electrical visibility of 98% at the optimal threshold. The overall fidelity of 97% is limited by thermal broadening of the Fermi distribution in the island of the readout SET. Our electron temperature is estimated to be $T_{el} \approx 100$ mK.

For the nuclear qubit measurement fidelity we use the same methods as in Ref. [4]. A single nuclear qubit readout is obtained from 50 single-shot readouts of the electron state after a nuclear-spin-dependent electron π-pulse. The limiting factor to the nuclear readout fidelity is given by the possibility of a random nuclear flip during the relatively long readout time. The nuclear lifetimes were 2900 s for the $|\Downarrow\rangle$ state and 7900 s for the $|\Uparrow\rangle$ state. Using the total readout time of 250 ms (50×5 ms) we get the measurement fidelity quoted in the main text and in the figures (we always quote the worst-case scenario of the shortest-lived nuclear state). All these values were measured on Device A.

The control fidelities of the 3 different qubits (electron, neutral nucleus and ionized nucleus) were all extracted using the method presented in Ref. [8]. By comparing the decays of a CPMG sequence with a CP, the pulse-error component of the decay can be extracted. Assuming Gaussian-distributed pulse errors, the decay is of the form:

$$P(N) \propto \exp\left(-(\sigma N/2)^2\right), \tag{1}$$

where σ is the standard variation of the rotation angle (in radians) with a mean of π, and N the number of pulses. To extract the control fidelity, we first apply a CPMG sequence with a fixed τ_{wait} and extract T_2^{CPMG} and the exponent n. We then apply a CP sequence with the same τ_{wait} and fit the decay to:

$$P(t_p) \propto \exp\left(-\left(\frac{t_p}{T_2^{\mathrm{CPMG}}}\right)^n\right) \exp\left(-\left(\frac{\sigma t_p}{2(\tau_{wait} + \tau_\pi)}\right)^2\right), \tag{2}$$

where $t_p = N(\tau_{wait} + \tau_\pi)$ is the total precession time between the initial and final $X_{\pi/2}$ pulses, and τ_π is the duration of each π-pulse. In the practice, we usually found that the value of T_2^{CPMG} was so long that the term $\exp\left(-(t_p/T_2^{\mathrm{CPMG}})^n\right)$ could be approximated with 1. After extracting σ from the fit of Eq. 2 to the CP decay data, we define the effective control fidelity as:

$$F_c^e = \frac{1}{2}[\cos(\sigma) + 1]. \tag{3}$$

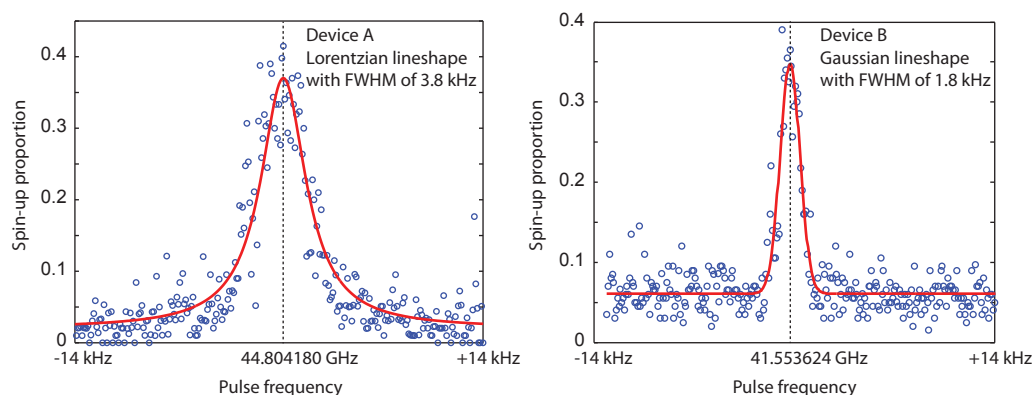Data from the CP sequences used to extract the control fidelity is shown in Fig. S2.

FIG. S1. **Direct measurement of electron spin resonance linewidths.** The ESR measurements were performed with -50 dBm of MW source power and 500 μs pulse width. Device A was measured using square–shaped pulses, while device B was measured using Gaussian–shaped pulses. Solid lines are a Lorentzian fit (Device A) and a Gaussian fit (Device B), with parameters as quoted in the figures.
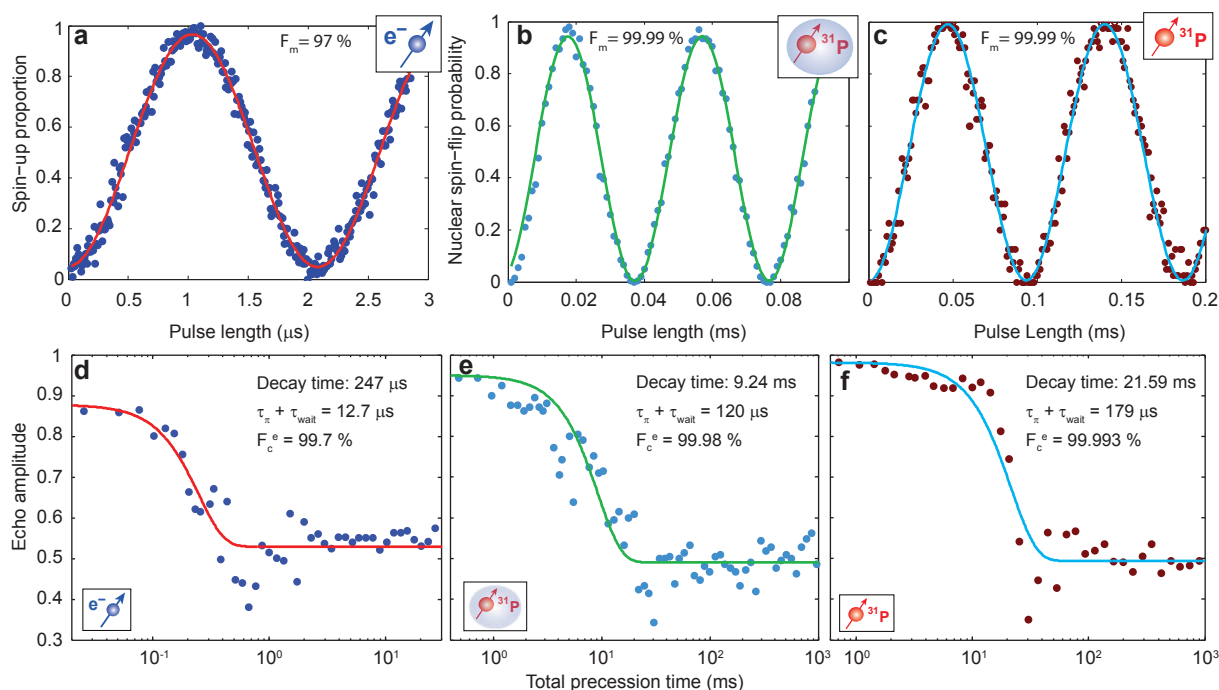

FIG. S2. **Qubit measurement and control fidelities. a-c** High-resolution Rabi oscillations for the electron (a), the neutral $^{31}P^0$ nucleus (b) and the ionized $^{31}P^+$ nucleus (c). The measurement (F_m) fidelities quoted in the figures were extracted from these data sets. **d-f** Carr-Purcell (CP) measurements to extract the qubit control fidelities. The CP echo decays were measured on the electron (d), the neutral nucleus (e) and the ionized nucleus (f) by applying π-pulses along the x-axis at short intervals. In this pulse sequence, the decay is dominated by the accumulation of pulse errors. The qubit control fidelity is extracted from the fits as described in the text.

E. Details of the noise spectroscopy method

Dynamical decoupling is a well-known method to cancel out low-frequency noise. By applying π-pulses at regular intervals (τ), the noise at frequencies much lower than $1/2\tau$ is effectively averaged out. For random noise with a mean of zero, noise at much higher frequencies also averages to zero. As a result it is possible to describe dy-

namical decoupling (DD) pulsing schemes as band-pass spectral filters for the noise [9–11]. Considering pure dephasing noise with a Hamiltonian:

$$\mathcal{H} = \frac{\hbar}{2}\left[\Omega + \beta(t)\right]\sigma_z, \qquad (4)$$

where Ω is the Larmor frequency ($\hbar\Omega$ is the energy splitting of the qubit states) and $\beta(t)$ is time-dependent noise (in angular frequency units), it can be shown [12–14] that

the decay of the coherence is of the form:

$$P(N\tau) \propto \exp\left(-\int_0^\infty S(\omega)|F(\omega, N\tau)|^2 d\omega\right), \quad (5)$$

where $S(\omega) = \int_{-\infty}^\infty \exp(-i\omega t)\langle\beta(t)\beta(0)\rangle dt$ is the power spectral density (PSD) of the noise and $|F(\omega, N\tau)|^2$ is a pulse sequence dependent function known as the filter function, since it determines which parts of the noise spectrum contribute to the decoherence process. The total evolution time is $N\tau$, where N is the number of pulses. The pulses are assumed to be instantaneous. We define $S(\omega)$ as the noise power in the energy splitting of the qubit states (in angular frequency units), as opposed to making assumption on its physical nature (magnetic, electric, etc.) and adding a coupling constant in Eq. (5).

The filter function $F(\omega, N\tau)$ has an analytical expression for the case of π-pulses applied at regular intervals [10]

$$|F(\omega, N\tau)|^2 = \frac{8}{\pi\omega^2}\frac{\sin^4(\omega\tau/4)\sin^2(\omega N\tau/2)}{\cos^2(\omega\tau/2)}. \quad (6)$$

This has been plotted in Fig. S3 with a constant interval between the pulses (top) and with a constant total evolution time (bottom). The top figure is relevant for the noise spectroscopy (Fig. 4b in the main text) whereas the bottom one describes how the passband frequency moves with increasing N at constant total evolution time (Fig. 4c in the main text).

Notably, if one keeps the total free evolution time of the qubit constant, the integral over the filter function is the same for all regular-interval π-pulsing schemes. Hence, if the dephasing noise has a fully flat (white) spectral density, the refocusing pulses will bring no improvement to the coherence time. Conversely, DD can be very effective in the presence of a frequency-dependent noise with decreasing power at higher frequencies. The power-law of the exponential decay will also depend on the shape of the dephasing noise within the "band" of the filter, giving exponential decay ($n = 1$) for white noise, gaussian decay ($n = 2$) for $1/\omega$ noise, and so on, i.e. $S(\omega) \propto \omega^{-(n-1)}$.

It was recently pointed out [10, 13, 14] that in the limit where N is large, the filter function becomes a series of delta functions and the coherence decay has a simple analytic form:

$$P(t) \propto \exp\left(-t\frac{4}{\pi^2}\sum_{k=0}^\infty \frac{1}{(2k+1)^2}S(\omega_k)\right), \quad (7)$$

where $\omega_k = (2k+1)\pi/\tau$. Hence, as proposed in [14], measuring the decay time T_2^S at multiples of some minimum frequency ω_0 (we chose $\omega_0/2\pi = 1$ kHz) allows one to map out the noise spectral density, including the higher harmonics of the filter function. We note that taking only the first term of Eq. (7) leads to the simple band-pass filter form, whereas in the case of frequency-independent noise ($S(\omega) = S$), Eq. (7) reduces to $P(t) \propto \exp(-tS/2)$.
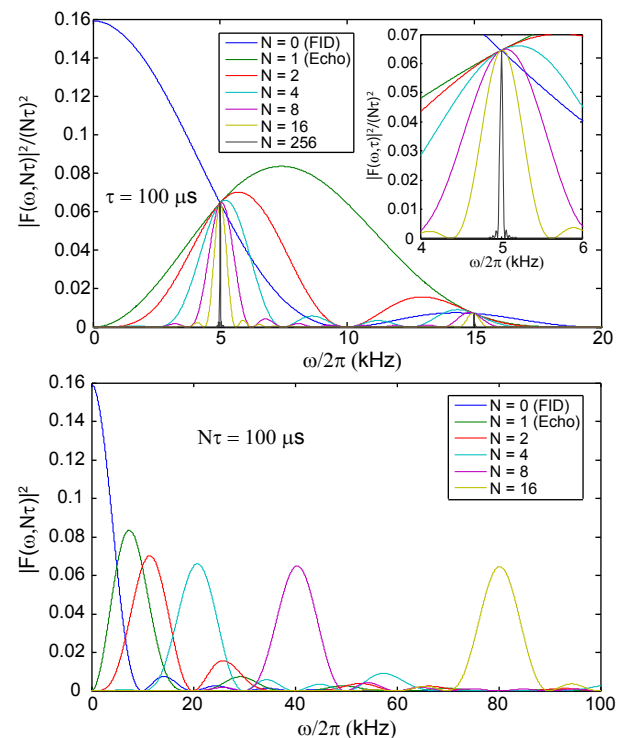

FIG. S3. **Dynamical decoupling filter functions.** Noise filter function of the CPMG sequence, plotted with fixed interval between the pulses (top) and with fixed total evolution time (bottom). The top plot is normalized with $(N\tau)^2$, as the height of the peak grows with the square of the total evolution time. (The width of the peak scales roughly as $(N\tau)^{-1}$.) In the bottom plot no normalization is needed, since the area under the curve stays constant.

F. Quantitative analysis of the possible sources of noise

1. Broadband noise

(i) Room-temperature thermal noise. We have performed extensive modeling of the electric and magnetic fields induced by the broadband antenna. The MW antenna is designed to produce no electric fields – hence the short-circuit termination of the co-planar stripline conductors. In practice, imperfections in the propagation along the antenna may result in nonzero electric fields at its termination. The electric field couples to the qubit energy levels by Stark-shifting the hyperfine constant A [15–17] and/or the g-factor of the electron spin [18]. Ideally, the antenna should also produce purely transverse oscillating magnetic field $B_1 \perp Z$. However, our device geometry does allow for some nonzero longitudinal field component.

For the modeling we assume a donor location in the middle of the implant window, 10 nm below the Si/SiO$_2$ interface, and model the electric and magnetic fields at that location using CST Microwave Studio finite-

elements software. The simulation results are shown in Fig. S4**a**.

For device A we measured a noise floor of $S(\omega) \approx 10$ rad^2/s, which converted to amplitude spectral density and to magnetic field gives $b_n = \hbar\sqrt{S(\omega)}/(g\mu_B) = 18$ pT/$\sqrt{\text{Hz}}$ for $g = 2$. The finite-elements modeling shows that, at $\sim$ kHz frequencies, 1 mW of power result in a longitudinal magnetic field component $B_z \approx 1$ mT. Since the magnetic field is proportional to the square root of the power, we deduce that the noise power P_n entering the MW antenna to produce $b_n = 18$ pT/$\sqrt{\text{Hz}}$ is:

$$P_n = \left(\frac{b_n}{1 \text{ mT}}\right)^2 \times 1 \text{ mW} = 3.2 \times 10^{-19}\text{W} = -155 \text{ dBm} \tag{8}$$

During the measurement of device A we had a total of 6 dB attenuation along the signal line (the losses of the coaxial cable are negligible at kHz frequencies), thus -155 dBm at the chip corresponds to $P_n^s = -149$ dBm noise power at the source. The power radiated down by the attenuators themselves would give maximum 2% correction to this value as they are thermalised to the pot (1.5 K) and mixing chamber (0.02 K). If we assume that the noise power is Johnson-Nyquist noise produced by a resistor R at $T = 300$ K, $P_n^s = 4k_BTR$ per unit of frequency, we find:

$$R = \frac{10^{-14.9} \times 10^{-3}}{4k_BT} = 76 \ \Omega. \tag{9}$$

This value is remarkably close to the 50 Ω impedance presented by the output of the microwave source, especially considering that the exact conversion between P_n and b_n involves the large uncertainty of the donor location.

When measuring Device B we increased the attenuation of the microwave line by 7 dB, and observed accordingly a decrease of the white noise floor, albeit not by the numerical amount expected on the basis of the additional attenuation. This could be due to a different donor location in Device B, such that the B_z component is larger than for device A.

Room temperature thermal noise should have a constant spectral density well beyond the electron spin Larmor frequency ~ 50 GHz. In this case, the transverse component of the magnetic noise would cause a T_1 (spin relaxation) process. The reason why a shortened T_{1e} is not observed is the frequency-dependent attenuation of the semi-rigid coaxial cable, which introduces a further ~ 30 dB attenuation at 50 GHz.

We note that the longitudinal component of the magnetic field produced by the microwave antenna could be eliminated completely by rotating the sample by 90°. If the external magnetic field B_0 were applied *along* the direction of the short-circuit termination of the antenna, then B_1 would always be perpendicular to B_0, irrespective of the donor depth. This rotated mounting requires a redesign of the sample enclosure and printed circuit board, and we intend to test it in future experiments.

(ii) Evanescent-wave Johnson noise (EWJN). In close proximity to metal surfaces the evanescent wave contribution to thermal and quantum fluctuations of the electromagnetic fields can be $\sim$20 orders of magnitude above the expected blackbody radiation levels. This phenomenon goes under the name of evanescent wave Johnson noise (EWJN) and has been identified as a major source of decoherence and heating of atoms trapped in vacuum near metal surfaces [19, 20]. Similar effects can arise in gated semiconductor devices, even at very low temperatures, through the quantum fluctuations of the electromagnetic fields in the metallic gate electrodes [21–23]. In the simplest case of an infinite half-space at the so-called quasi-static limit (applicable to our geometry) the magnetic field fluctuations have a relatively simple form: [19, 21]

$$S_B^i(\omega) = s_i \frac{\sigma\hbar\omega}{32\pi\epsilon_0^2 c^4 z} \coth\left(\frac{\hbar\omega}{2k_BT}\right), \tag{10}$$

where σ is the conductance of the metal, ϵ_0 the vacuum permittivity, c the speed of light, z the distance from the surface and s_i is $1/2$ for x- and y-components of the field and 1 for z component. The surface is assumed to lie in the x-y plane, and our static magnetic field would be in the x-direction in this geometry.

Using the measured low-temperature conductivity of the aluminium used for the MW antenna ($\sigma = 1.4 \times 10^8$ S/m) [24], the noise floor measured in Device A could be produced by an infinite surface at $T = 150$ mK, if $z = 15$ nm. Although our gates are obviously not an infinite plane, these values are not wholly unreasonable. However, we consider this explanation unlikely since Eq. 10 is in total contradiction with our measured energy relaxation (T_{1e}) time. The T_{1e} time is proportional to the (transverse) magnetic field noise at Larmor frequency of the qubit. Based on this, the same parameters predict a T_{1e} time of the order of 10 ms, whereas the measured value was around 6 s, a discrepancy of almost three orders of magnitude.

We emphasize that this is not just a matter of choosing the right parameters: unlike the case of room-temperature Johnson noise reaching the qubit through a line with a strongly frequency-dependent attenuation, EWJN is generated locally and it has an Ohmic frequency dependence in the regime $\hbar\omega > k_BT$. Hence, at low temperatures it generally predicts the decoherence to be dominated by the T_{1e} time [23], which is not the case in our qubits. The same arguments also apply if we assume that the noise floor would be electric field noise, coupling to our spin due to isotropic hyperfine interaction.

With the data at hand, we consider room-temperature Johnson noise more likely to play a role than EWJN. Future experiments, where further attempts will be made to reduce the effect of room temperature noise, might help verifying whether EWJN becomes apparent under certain circumstances.
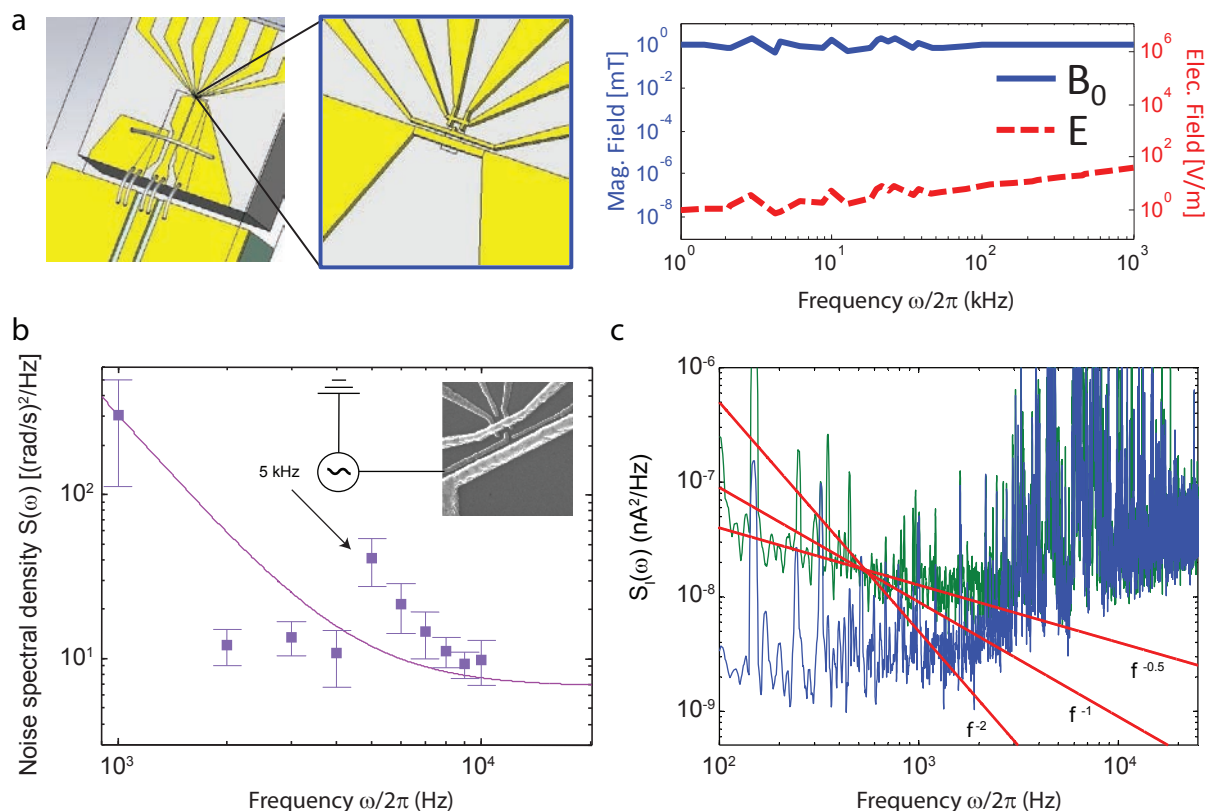
FIG. S4. **Analysis of noise sources. a,** The left drawing shows the geometry used for the MW antenna. The simulation results are shown in the right panel for the longitudinal magnetic field component (B_0) and electric field (E), at low frequencies. All plots are calculated by assuming an input signal of 0 dBm at each modeled frequency. Calculations of the magnetic and electric fields produced by the MW antenna were performed using the finite-elements electromagnetic solver CST Microwave Studio. **b,** Noise spectroscopy measurement while applying a 200 μV peak-to-peak sinusoidal voltage at 5 kHz to the gate shown in the SEM image. A clear peak appeared in the noise spectra at 5 kHz. The solid line is the same as plotted in Fig. 4**a** of the main text. **c,** Power spectral density of current traces taken while the SET was tuned to be either maximally sensitive to charge fluctuations (green, top) or minimally sensitive (blue, bottom). The data has been numerically smoothed. The difference between green and blue traces at low frequencies reveals the charge noise in the device. Its spectrum is of the form $1/\omega^\alpha$, with $\alpha \approx 0.5$. Lines are guides to the eye. At higher frequencies (above ~ 2 kHz) the noise is dominated by the room-temperature transimpedance amplifier and the two curves coincide.

2. Low-frequency noise $S(\omega) \propto 1/\omega^{2.5}$

The low-frequency, coloured part of the noise coupling to the electron spin is of the form $S(\omega) \propto 1/\omega^{2.5}$. This is the form of noise that could most realistically be attributed to interface effects, such as electric or magnetic noise from charge fluctuators and paramagnetic traps. Below we analyse sources of coloured noise that could conceivably exist in our nanoelectronic device.

(i) Electric fields – charge and gate noise. Electric field noise can be generated by charge fluctuations intrinsic to the device (two-level fluctuators, dangling bonds, etc.), or by noise voltages on the gates. Since we do not have a means to distinguish between them, we discuss these contributions together under the generic term of electric field noise.

First of all, we verified experimentally that the e$^-$ qubit is potentially sensitive to electric fields. We re-

peated the measurement of $S(\omega)$ for frequencies between 1 and 10 kHz while applying a 5 kHz sine-wave voltage signal on one of the control gates fabricated above the donor implant window. The choice of 5 kHz frequency was to facilitate the observation of the noise peak, by working where the intrinsic noise background has reached its lowest plateau. The data is presented in Fig. S4**b**. A clear peak in $S(\omega)$ appeared at the expected 5 kHz frequency, confirming the effectiveness of the spectroscopy method, and the presence of some degree of Stark-shift of A and/or g. However, the amplitude of the signal we had to apply in order to distinguish it from the background was of the order of 100 μV, much above what could be conceivably produced by charge fluctuations of two-level systems at the Si/SiO$_2$ interface.

Even more convincingly, decoherence from electric field noise can be ruled out on the basis of its spectral fingerprint. We measured the spectrum of the intrinsic electric field noise in our device by acquiring long traces of I_{SET},

first while the device was tuned to a slope of a Coulomb peak, where the current through the SET is maximally sensitive to any charge variations in its surroundings, and then while the SET was in Coulomb blockade, where the only measured signal is the noise of the amplifier chain. Comparing the spectra of these two traces we can extract the low-frequency electrical noise within the device (at higher frequencies the noise floor of the amplifier is the limiting noise). As shown in Fig. S4c, the low-frequency noise follows an $1/\omega^\alpha$ curve with $\alpha \approx 0.5$. This allows us to conclude that the $1/\omega^{2.5}$ noise component observed in the qubit spectroscopy is not due to electric fields, whether of intrinsic (charge fluctuators) or extrinsic (gate noise) origin.

(ii) **Paramagnetic spin fluctuations**. Interface traps can carry a paramagnetic spin, the fluctuations of which may produce magnetic field noise at the qubit location. Some evidence for this phenomenon has been reported in the literature, when studying the coherence of donor spins near a Si/SiO$_2$ interface [25, 26]. All of the existing literature reports experiments carried out in the high-temperature limit, $\gamma_e B_0 \ll k_B T$ (usually $B_0 \approx 0.35$ T and $T \approx 5$ K). On the contrary, our experiments are conducted in the low-temperature limit, $\gamma_e B_0 \gg k_B T$ ($B_0 \approx 1.5$ T and $T \approx 0.1$ K), where spin fluctuations are exponentially suppressed. Very generally, the high-temperature limit of a decoherence rate $T_2^{-1}(k_B T \gg \gamma_e B_0)$ caused by coupling to paramagnetic spins scales to lower temperatures as [27, 28]

$$T_2^{-1}(B_0, T) \approx T_2^{-1}\left(k_B T \gg \gamma_e B_0\right) \sqrt{1 - P_e^2}, \quad (11a)$$

$$P_e = \tanh^2\left(\frac{\gamma_e B_0}{2 k_B T}\right), \quad (11b)$$

where P_e is the equilibrium thermal polarization of the electron spins. This applies to spin fluctuations caused both by spin-lattice relaxation (T_1) [29] and spin-spin coupling processes (T_2) [30]. For an electron spin in silicon ($\gamma_e \approx 28$ GHz/T) at $B_0 \approx 1.5$ T and $T \approx 0.1$ K we find $\sqrt{1 - P_e^2} \approx 9 \times 10^{-5}$. Our spin readout method does not allow us to measure T_2 in the high-temperature limit. However we can take the value of $T_2^{\mathrm{H}}(k_B T \gg \gamma_e B_0) \approx 1.3$ μs from Paik *et al.* [26] as the most extreme example of interface-trap-limited coherence time, since that experiment was based on spin-dependent recombination of donor-bound carriers with interface traps, and therefore was explicitly sensitive only to donors very close to a paramagnetic trap. From Eq. 11 we infer that the same experiment carried out at $B_0 \approx 1.5$ T and $T \approx 0.1$ K would yield $T_2^{\mathrm{H}} > 15$ ms, already an order of magnitude longer than what we observed. Since the ^{31}P donor in our devices is much less likely to be so strongly coupled to a paramagnetic trap as compared to the device of Paik *et al.*, we conclude that magnetic noise from paramagnetic traps is not relevant to our experiment. We also note that the SiO$_2$ in our devices is of very high quality, with a typical trap density $\sim 10^{10}$/eV/cm^2 [31].

(iii) **Proton nuclear spins**. Another potential source of interface-related coloured noise could be the spectral diffusion caused by proton (^{1}H) spins in the hydrogen atoms present in the SiO$_2$ and at the interface. In our devices, H atoms are introduced in the oxide during the forming gas anneal step, with the aim of passivating traps at the Si/SiO$_2$ interface. A reasonable estimate of their density would be the typical density of interface traps before the anneal step, of order $n_{2D} \sim 10^{12}$/cm^2, corresponding to an average distance $\bar{d} = 0.5 n_{2D}^{-1/2} \sim 5$ nm. De Sousa [29] calculated the coherence time for a donor spin placed under a hydrogen-terminated Si surface, i.e. under a monolayer of ^{1}H which form a square lattice of side 3.84 Å. The predicted T_{2e} is of order 1 ms for a 10 nm deep donor. The ^{1}H spin polarization remains very small even at the high-field and low-temperature of our experiment, therefore the proton spin fluctuations are not thermally suppressed. Since the ^{1}H spin noise arises from their dipolar interaction, T_2 should scale like $\bar{d}^3$, thus increasing by a factor $(5/0.384)^3 \sim 2,000$ for random protons at 10^{12}/cm^2 concentration. Further, we argue that the calculation of de Sousa should be taken as an extreme lower bound to the true coherence time allowed by this process, since it assumes that all ^{1}H spins have *exactly* the same resonance frequency, and therefore can freely undergo energy-conserving spin fluctuations mediated by their (weak) dipolar coupling. In our devices, proton spins at various random locations in the SiO$_2$ and at the Si/SiO$_2$ interface will certainly experience significant Stark and chemical shifts, which further suppress the rate of dipolar flip-flop transitions by several orders of magnitude [30]. Therefore we consider ^{1}H nuclear spins extremely unlikely to play a role in our experiment.

(iv) **Superconducting magnet noise**. The Larmor precession frequency of the electron spin qubit is determined by the Zeeman energy, $h\gamma_e B_0$, where B_0 is the static magnetic field. In our experimental setup, B_0 is produced by a 4-inch bore NbTi superconducting magnet. Therefore, noise in B_0 will feed directly into the coherence of the qubit.

The presence of coloured noise from superconducting magnets has been reported in the context of ion-trap qubits. In Refs. [32, 33] a high-homogeneity NMR magnet was used to produce a 4.5 T field applied to ^{9}Be$^+$ ions in a Penning trap. The magnetic noise spectrum was measured directly, and observed to scale as $S(\omega) \sim \omega^{-4}$. Ramsey T_{2e}^* and Hahn echo T_{2e}^{H} coherence times in the ^{9}Be$^+$ ions were a factor ~ 10 longer than the ones measured in our e$^-$ qubit. Since both types of qubits have $\gamma_e \approx 28$ GHz/T, attributing the low-frequency decoherence in our system to magnet noise requires assuming a ~ 10 times stronger noise in our magnet as compared to the one used in Refs. [32, 33]. This is quite reasonable, since our magnet is a wide-bore, low homogeneity solenoid not optimized for spin resonance experiments.

The physical origin of the noise in superconducting magnets is being investigated by several groups. Current hypotheses are the role of flux creep, or mechanical vibrations while the qubit is not placed exactly in the magnet

centre. We have repeatedly observed increased noise levels during and after a liquid helium refill, which could indeed cause enhanced flux creep, or enhanced motion of the magnet caused by the helium boil-off. We have also observed that the Ramsey fringes become substantially more noisy if the persistent mode switch is open, which indicates that the power supply noise can be significant.

If T_{2e}^* and T_{2e}^{H} are limited by magnetic field noise, then the ionized-nucleus T_{2n+}^* and T_{2n+}^{H} values should be longer than the electron ones by the ratio $\gamma_e/\gamma_n = 1623$. Remarkably, on Device B we found $T_{2n+}^{\mathrm{H}}/T_{2e}^{\mathrm{H}} = 1636$. For the Ramsey decay, and for Device A, the ratios are within a factor ~ 2 of the expected value. The neutral donor shows much shorter coherence times, which indicates that another (unknown) mechanism is at play there, most likely involving the electron spin.

Finally, a recent ESR experiment on a single Si quantum dot (fabricated on the same ^{28}Si substrate as the devices discussed here) has given very similar values of T_{2e}^* and T_{2e}^{H} as the donor devices [34]. The dot-based and donor-based devices differ quite significantly in term of confining potential, gate layout, proximity to the Si/SiO$_2$ interface, and sensitivity of the resonance frequency to electric fields. However, both devices were measured with (nominally) identical magnets and identical power supplies. Therefore, if the Ramsey and Hahn coherence times are limited by magnet noise, they should be similar in both devices, as indeed observed.

3. Concluding remarks on noise

There is a vast number of possible sources of noise in a nanoscale electronic device. Our experiments make a compelling case for excluding noise sources arising from the proximity of the qubit to the Si/SiO$_2$ interface. This is one of the main messages of our work.

Identifying the true sources of noise is of course much more difficult than excluding others. In the discussion above we have attempted to analyze all the noise sources we are aware of, and we concluded that the most likely scenario, with the data we have at hand, is: (i) the low-frequency noise $\propto 1/\omega^{2.5}$ is produced by the superconducting magnet; (ii) the constant high-frequency noise floor is caused by the magnetic field component of the thermal radiation leaking from room temperature to the tip of the microwave antenna. Future experiments on new devices, with different gate layout and different sample mounting, and possibly conducted in new dilution refrigerators with different magnets, will help further elucidate these issues.

[1] Pla, J. J., Tan, K. Y., Dehollain, J. P., Lim, W. H., Morton, J. J. L., Jamieson, D. N., Dzurak, A. S. & Morello, A. A single-atom electron spin qubit in silicon. *Nature* **489**, 541–545 (2012).

[2] Saeedi, K., Simmons, S., Salvail, J. Z., Dluhy, P., Riemann, H., Abrosimov, N. V., Becker, P., Pohl, H.-J., Morton, J. J. L. & Thewalt, M. L. W. Room-temperature quantum bit storage exceeding 39 minutes using ionized donors in silicon-28. *Science* **342**, 830–833 (2013).

[3] Morello, A. *et al.* Single-shot readout of an electron spin in silicon. *Nature* **467**, 687–691 (2010).

[4] Pla, J. J., Tan, K. Y., Dehollain, J. P., Lim, W. H., Morton, J. J. L., Zwanenburg, F. A., Jamieson, D. N., Dzurak, A. S. & Morello, A. High-fidelity readout and control of a nuclear spin qubit in silicon. *Nature* **496**, 334–338 (2013).

[5] Tyryshkin, A. M. *et al.* Electron spin coherence exceeding seconds in high-purity silicon. *Nat. Mater.* **11**, 143–147 (2012).

[6] Saraiva, A., Baena, A., Calderón, M. & Koiller, B. Theory of one and two donors in silicon. *arXiv preprint arXiv:1407.8224* (2014).

[7] Dobrovitski, V., Feiguin, A., Awschalom, D. & Hanson, R. Decoherence dynamics of a single spin versus spin ensemble. *Physical Review B* **77**, 245212 (2008).

[8] Morton, J. J. L., Tyryshkin, A. M., Ardavan, A., Porfyrakis, K., Lyon, S. A. & Briggs, G. A. D. Measuring errors in single-qubit rotations by pulsed electron paramagnetic resonance. *Phys. Rev. A* **71**, 012332– (2005).

[9] Uhrig, G. S. Keeping a quantum bit alive by optimized π-pulse sequences. *Phys. Rev. Lett.* **98**, 100504 (2007).

[10] Cywinski, L., Lutchyn, R. M., Nave, C. P. & Das Sarma, S. How to enhance dephasing time in superconducting qubits. *Phys. Rev. B* **77**, 174509 (2008).

[11] Biercuk, M. J., Doherty, A. C. & Uys, H. Dynamical decoupling sequence construction as a filter-design problem. *Journal of Physics B: Atomic, Molecular and Optical Physics* **44**, 154002 (2011).

[12] Bylander, J., Gustavsson, S., Yan, F., Yoshihara, F., Harrabi, K., Fitch, G., Cory, D. G., Nakamura, Y., Tsai, J.-S. & Oliver, W. D. Noise spectroscopy through dynamical decoupling with a superconducting flux qubit. *Nature Physics* **7**, 565–570 (2011).

[13] Yuge, T., Sasaki, S. & Hirayama, Y. Measurement of the noise spectrum using a multiple-pulse sequence. *Phys. Rev. Lett.* **107**, 170504 (2011).

[14] Alvarez, G. A. & Suter, D. Measuring the spectrum of colored noise by dynamical decoupling. *Phys. Rev. Lett.* **107**, 230501 (2011).

[15] Bradbury, F. R., Tyryshkin, A. M., Sabouret, G., Bokor, J., Schenkel, T. & Lyon, S. A. Stark tuning of donor electron spins in silicon. *Phys. Rev. Lett.* **97**, 176404– (2006).

[16] Rahman, R., Wellard, C. J., Bradbury, F. R., Prada, M., Cole, J. H., Klimeck, G. & Hollenberg, L. C. High precision quantum control of single donor spins in silicon. *Phys. Rev. Lett.* **99**, 036403 (2007).

[17] Mohiyaddin, F. A., Rahman, R., Kalra, R., Klimeck, G., Hollenberg, L. C. L., Pla, J. J., Dzurak, A. S. & Morello, A. Noninvasive spatial metrology of single-atom devices. *Nano Lett.* **13**, 1903–1909 (2013).

[18] Rahman, R., Park, S. H., Boykin, T. B., Klimeck, G.,

Rogge, S. & Hollenberg, L. C. L. Gate-induced *g*-factor control and dimensional transition for donors in multivalley semiconductors. *Phys. Rev. B* **80**, 155301– (2009).

[19] Henkel, C., Pötting, S. & Wilkens, M. Loss and heating of particles in small and noisy traps. *Applied Physics B* **69**, 379–387 (1999).

[20] Harber, D., McGuirk, J., Obrecht, J. & Cornell, E. Thermally induced losses in ultra-cold atoms magnetically trapped near room-temperature surfaces. *J. Low Temp. Phys.* **133**, 229–238 (2003).

[21] Langsjoen, L. S., Poudel, A., Vavilov, M. G. & Joynt, R. Qubit relaxation from evanescent-wave johnson noise. *Physical Review A* **86**, 010301 (2012).

[22] Poudel, A., Langsjoen, L. S., Vavilov, M. G. & Joynt, R. Relaxation in quantum dots due to evanescent-wave johnson noise. *Physical Review B* **87**, 045301 (2013).

[23] Langsjoen, L. S., Poudel, A., Vavilov, M. G. & Joynt, R. Electromagnetic fluctuations near thin metallic films. *Phys. Rev. B* **89**, 115401 (2014).

[24] Dehollain, J. P., Pla, J. J., Siew, E., Tan, K. Y., Dzurak, A. S. & Morello, A. Nanoscale broadband transmission lines for spin qubit control. *Nanotechnology* **24**, 015202 (2013).

[25] Schenkel, T., Liddle, J., Persaud, A., Tyryshkin, A., Lyon, S., de Sousa, R., Whaley, K. B., Bokor, J., Shangkuan, J. & Chakarov, I. Electrical activation and electron spin coherence of ultralow dose antimony implants in silicon. *Appl. Phys. Lett.* **88**, 112101–112101 (2006).

[26] Paik, S.-Y., Lee, S.-Y., Baker, W., McCamey, D. & Boehme, C. t_1 and t_2 spin relaxation time limitations of phosphorous donor electrons near crystalline silicon to silicon dioxide interface defects. *Physical Review B* **81**, 075214 (2010).

[27] Morello, A., Stamp, P. & Tupitsyn, I. S. Pairwise decoherence in coupled spin qubit networks. *Phys. Rev. Lett.* **97**, 207206 (2006).

[28] McMillan, M. & Opechowski, W. On the temperature dependence of the shape of paramagnetic resonance lines. *Canadian J. Phys.* **38**, 1168–1186 (1960).

[29] De Sousa, R. Dangling-bond spin relaxation and magnetic $1/f$ noise from the amorphous-semiconductor/oxide interface: Theory. *Physical Review B* **76**, 245306 (2007).

[30] Witzel, W. M., Carroll, M. S., Morello, A., Cywinski, L. & Das Sarma, S. Electron spin decoherence in isotope-enriched silicon. *Phys. Rev. Lett.* **105**, 187602 (2010).

[31] Johnson, B., McCallum, J., Willems van Beveren, L. & Gauja, E. Deep level transient spectroscopy study for the development of ion-implanted silicon field-effect transistors for spin-dependent transport. *Thin Solid Films* **518**, 2524–2527 (2010).

[32] Biercuk, M. J., Uys, H., VanDevender, A. P., Shiga, N., Itano, W. M. & Bollinger, J. J. Optimized dynamical decoupling in a model quantum memory. *Nature* **458**, 996–1000 (2009).

[33] Biercuk, M. J., Uys, H., Vandevender, A. P., Shiga, N., Itano, W. M. & Bollinger, J. J. High-fidelity quantum control using ion crystals in a penning trap. *Quantum Information & Computation* **9**, 920–949 (2009).

[34] Veldhorst, M. *et al.* An addressable quantum dot qubit with fault-tolerant control fidelity. *arXiv:1407.1950* (2014).